Optimization of pixel size and propagation distance in X-ray phase-contrast virtual histology

S. Donato,[a,b,*] **L.M. Arana Peña,**[c,d,e] **D. Bonazza,**[f] **V. Formoso,**[a,g,h] **R. Longo,**[c,d] **G. Tromba**[e] **and L. Brombal**[d]

[a] *Department of Physics and STAR-LAB, University of Calabria, via P. Bucci 31C, Rende (CS), I-87036, Italy*
[b] *INFN — Sezione di Frascati, via E. Fermi 54, Frascati I-00044, Italy*
[c] *Department of Physics, University of Trieste, Via Alfonso Valerio 2, Trieste, I-34127, Italy*
[d] *INFN — Sezione di Trieste, Via Alfonso Valerio 2, Trieste, I-34127, Italy*
[e] *Elettra-Sincrotrone Trieste S.C.p.A., s.s. 14-km 163.5 in AREA Science Park, Basovizza, Trieste, I-34149, Italy*
[f] *Surgical Pathology Unit, Cattinara Hospital, Azienda Sanitaria Universitaria Giuliana Isontina (ASUGI), Strada di Fiume, 447, Trieste, I-34149, Italy*
[g] *CNISM — Via della Vasca Navale, 84, Roma RM, I-00146, Italy*
[h] *CNR–Nanotec, University of Calabria, Via P. Bucci 31C, 87036 Rende (CS), I-87036, Italy*

E-mail: sandro.donato@fis.unical.it

Abstract: X-ray phase-contrast coupled to high-spatial resolution imaging systems provides a high sensitivity for distinguishing soft tissue structures in small samples, thus being suited for X-ray virtual histology. Propagation-based phase-contrast tomography can deliver a considerable gain in signal-to-noise ratio (SNR) at small pixel sizes when it is combined to a suitable phase retrieval filter. We optimized acquisition parameters, namely the propagation distance and the pixel size, with the aim of providing adequate spatial resolution and sensitivity for virtual histology of breast surgery specimens, scanned with a phase-contrast microtomography (μCT) system employing a commercial sCMOS detector at the SYRMEP beamline of the Italian synchrotron facility Elettra (Trieste, Italy). A pathological breast tissue sample was embedded in paraffin and imaged using a polychromatic synchrotron beam at an average energy of 24 keV. The high numerical optical aperture of the imaging system enabled to adjust the pixel size to 1, 2.5 and 4 μm. The scans were acquired at five sample-to-detector distances: 4.5, 150, 250, 500 and 1000 mm. SNR was

*Corresponding author.

measured in an homogeneous region portion of the μCT image for each combination of pixel size and propagation distance. Experimental results were compared to a theoretical model taking into account the actual point spread function of the employed imaging system. The measured gain of SNR associated with the application of the phase-retrieval matched the predictions for large Fresnel numbers ($N_F > 2$). For each pixel size, an optimal range of propagation distances was found. Optimal μCT reconstructions were then compared with their respective histopatological images, showing an excellent visibility of relevant structures. The optimization performed in this study will allow to select the most appropriate geometrical configurations for future acquisitions of virtual histology images of different specimens via phase-contrast microtomography.

KEYWORDS: Computerized Tomography (CT) and Computed Radiography (CR); X-ray detectors; Inspection with X-rays

Contents

1 Introduction

The use of computed tomography at the micrometre scale (μCT) is becoming a viable solution in the field of virtual histology [1–3]. In principle, μCT can provide a complete three-dimensional visualization of surgical specimens which can be virtually sliced at any point and in any direction. This, if not a diagnostic tool per se, can enable guided sectioning of tissues in histological analysis for selecting the most suitable cutting plane when dissecting specimens in order to obtain, e.g., the largest cross-section of the pathological area of interest. One of the challenges of virtual histology is related to the poor X-ray attenuation contrast that exists between the soft tissues commonly encountered in biopsy specimens. In this context, the high sensitivity offered by X-ray phase-contrast imaging techniques [4, 5], such as propagation-based (PB) imaging, can overcome this limitation. To be suitable for clinical evaluation, virtual histology images should have a spatial resolution high enough to distinguish small structures but, at the same time, cover a sufficiently large volume to enable the inspection of biopsy specimens, usually having sizes of 4–5 cm^3, in a single or very few μCT acquisitions. Considering the standard dimensions of commercial detectors (4–8 MP), the aforementioned requests translate in acquisitions with pixel size of few microns (1–5 μm). To provide adequate visibility of soft tissue structures in the virtual slices, such high spatial resolutions must be combined with high signal-to-noise ratio (SNR).

In conventional attenuation-based μCT the image noise is strongly dependent on the detector pixel size and the geometrical magnification, thus limiting high-resolution applications in presence of constraints in terms of radiation dose or scan time. In these cases, and particularly for μCT on soft tissues, where the attenuation contrast between different components is small, images show a very low SNR. Phase-contrast imaging techniques have shown to dramatically enhance soft tissues contrast sensitivity without increasing the dose or the exposure time. The advantage of phase-contrast imaging over the conventional absorption imaging, for soft tissues in the energy range [10–100] keV, is based on the fact that the decrement from unity (δ) of the refraction index (n), responsible for phase effects, is about three orders of magnitude higher than the absorption

term (β), used in the conventional radiology [4]. Among the different phase-contrast techniques, PB is the simplest from an experimental point of view since it requires only to set the propagation distance between sample and detector. On the other hand, images acquired with the PB technique show an enhanced contrast in the tissue interfaces (i.e. edge-enhancement), which in the ray-optical approximation is proportional to the Laplacian of the object-induced phase-shift [6]. This edge-enhancement can be modelled as a high-spatial frequency boost in the Fourier space, thus an increase in the spatial resolution [7]. Edge-enhanced images are then further processed by the application of a phase-retrieval (PhR) algorithm, among which the Homogeneous Transport-of-Intensity Equation (TIE-Hom) [8], which assume the imaged object to have a constant δ/β ratio, is the most widely used. When compared to conventional attenuation-based imaging, the combination of free-space propagation and PhR results in an increase of SNR in reconstructed images while preserving spatial resolution and contrast [7, 9].

Recently published theoretical models [7, 10] showed that, in the near field regime, PB phase-contrast tomography along with the application of PhR, mitigates the dependence of noise on the pixel size bringing to a major SNR gain at small pixel sizes. Similarly, the model predicts a steep increase in the SNR for increasing propagation distances. In two recent papers [9, 11] this model was quantitatively compared with experimental results obtained with monochromatic synchrotron radiation and employing a photon-counting detector having a quasi-ideal (box-like) response function. The measured SNR gain due to the PhR application showed a good agreement with the theoretical prediction by varying both the pixel size and the propagation distance. This quantitatively demonstrated that a careful optimization in terms of pixel size and propagation distance is required to fully exploit the advantages of PB and PhR. On the other hand, at present the level of spatial resolution required by virtual histology cannot be achieved with photon-counting detectors. Another limitation in their use comes from the extremely high X-ray fluxes which are needed to provide high SNR at high resolution, that is commonly achieved at synchrotrons by employing white (i.e. polychromatic) beams. These features require the use of small-pixel indirect-conversion detectors, such as CCD or sCMOS, usually coupled with magnifying optical elements, leading to a detector's response function that is far from being a single-pixel wide box function. Both polychromaticity and wide response function represent deviations from the model validated in [11]. In this context, we present a preliminary experimental optimization of propagation distance and pixel size obtained in virtual histology experiments, with polychromatic beam and an indirect-conversion imaging system, performed at the SYRMEP beamline of the Italian synchrotron facility Elettra (Trieste, Italy). We performed tomographic acquisitions of a surgical breast specimen using three different pixel sizes and five different sample-to-detector distances. For each image, noise and SNR were measured within homogeneous regions of the sample and optimal combinations of pixel size and propagation distance were identified. Experimental results were compared to the theoretical model which has been adapted to the imaging system-specific point-spread function. This preliminary optimization will serve as guideline in the choice of the best experimental parameters for a future larger virtual histology study, aiming to assess the invasiveness of malignant diseases in various anatomical districts.

2 Materials and methods

2.1 Image noise model in propagation-based µCT

Nesterets and co-workers described mathematically the effect of PhR on µCT images proposing a model in which are included all the components part of the imaging chain in a tomographic experiment: from the geometrical configuration of the setup, to the characteristics of the detector and, finally, image reconstruction [10, 12]. More specifically, the model assumes a Poisson dominated detector noise, flat-fielded 2D projection images, stable source intensity and imaging setup, and a parallel beam geometry with reconstruction performed through the Filtered-Back-Projection (FBP) algorithm [10]. When measured in a homogeneous region portion of the µCT image acquired at a fixed fluence, the SNR can be expressed as:

$$\mathrm{SNR} \propto \frac{h^2}{M^2} \frac{1}{f(A; d/h)} \tag{2.1}$$

where, M is the geometric magnification, h the detector pixel size, $f(A;\, d/h)$ a dimensionless function that accounts for the tomographic process (filtering and interpolation), the detector's modulation transfer function (MTF) and the phase retrieval [11]. Additionally, d is the Full Width at Half Maximum (FWHM) of the detector's Point Spread Function (PSF). Specifically, the function $f(A;\, d/h)$ can be written as:

$$f(A; d/h) = 2\pi^2 \int_0^{1/2} \mathrm{d}U\, G^2(U) F_{\mathrm{int}}(U) \int_{-1/2}^{1/2} \mathrm{d}V\, \frac{\mathrm{MTF}^2(U, V; d/h)}{[1 + A(U^2 + V^2)]^2} \tag{2.2}$$

where $G(U)$ is the reconstruction filter, $F_{\mathrm{int}}(U)$ describes the effect on noise of the interpolation from polar to Cartesian coordinates in the back-projection process, $\mathrm{MTF}(U, V;\, d/h)$ is the detector MTF parametrized through the dimensionless quantity d/h, with d the full-width-at-half-maximum (FWHM) of the detector's point spread function (PSF), while U and V are dimensionless normalized frequencies. The parameter A depends on the refractive properties of the sample, on the setup geometry and on the detector pixel size as:

$$A = \pi \frac{\delta_1 - \delta_2}{\beta_1 - \beta_2} \lambda M \frac{R_2}{h^2} \tag{2.3}$$

where λ is the radiation wavelength, the subscripts 1, 2 in the δ and β terms refer to an interface between two materials having given different refractive indices, and R_2 is the sample-to-detector (or propagation) distance. When no PhR is applied ($A = 0$) the function f does not explicitly depend on pixel size h and magnification M, thus SNR is proportional to h^2/M^2 (see equation (2.1)) as known for conventional attenuation-based µCT. If PhR is applied ($A > 0$) the function f will result smaller, if compared to the case of $A = 0$, and consequently there is a gain in the SNR. The validity of the model applies in the near-field propagation regime, corresponding to large Fresnel numbers, i.e., $N_{\mathrm{F}} = d^2/(M^2 \lambda R_2) \gg 1$. In experimental practice this condition is often relaxed down to N_{F} slightly higher than 1.

2.2 Experimental acquisitions and data processing

Experiments were carried out by using the white-beam configuration mode available at the SYRMEP beamline. The X-ray beam is produced by a bending magnet resulting in a

spectrum in the energy range from 8.5 keV to 40 keV. To remove low energy components and reduce the beam-hardening effect, a filtration with 1 mm of Si was employed. The resulting beam had an average energy of 24 keV (considering the storage ring operating mode at 2.4 GeV). The sample was a surgical specimen of pathologic (intraductal papilloma) breast tissue embedded in paraffin and provided by the Pathology Unit of the Academic Hospital of Cattinara, Trieste University (Italy). PB images were acquired in the framework of the operative protocol of the Breast Unit of the Trieste University Hospital ("PDTA Neoplasia mammaria", approved on 11 December 2019 by ASUGI-Azienda Sanitaria Universitaria Giuliano Isontina, Italy). The protocol entails a written informed consent which is obtained from the patients before their inclusion into breast CT imaging studies. The imaging system was a Hamamatsu sCMOS camera (2048 × 2048 pixels) coupled with a GGG:Eu scintillator (thickness of 45 µm) and a high numerical aperture optic which enables to adjust the pixel size between 0.9 and 6.5 µm. In the study we used three different optical magnifications resulting in three pixel sizes (h): 1, 2.5 and 4 µm. We performed µCT scans for each pixel size, collecting 1800 projections over 180°, at 5 sample-detector distances (R_2): 4.5, 150, 250, 500 and 1000 mm, while the source-to-sample distance was constant at 22.3 m. The exposure time was set to 40 msec/projection resulting in an overall exposure of 72 s per scan. Projections were pre-processed by conventional dark-current subtraction, flat-fielding and ring artifact removal. Then the TIE-Hom-based phase-retrieval filter [8] was applied. The filter parameter, $\delta/\beta = (\delta_1 - \delta_2)/(\beta_1 - \beta_2)$, was set to 350 for all datasets. After processing, the final CT reconstruction yields a 3D map which is substantially proportional to the linear attenuation coefficient of the sample [13]. Tomographic reconstructions were performed by using a GPU-based FBP algorithm with linear interpolaton and Shepp-Logan filtering, meaning that in equation (2.2): $G(U) = U\,\mathrm{sinc}(U) = U\sin(\pi x)/(\pi x)$ and $F_{\mathrm{int}}(U) = [2 + \cos(2\pi U)]/3$. After reconstruction, µCT slices were processed via a de-trending procedure for an additional beam-hardening correction [14]. For each dataset, the gain of SNR ($\mathrm{SNR_{gain}}$) associated with the application of phase retrieval was measured within a homogeneous region filled by paraffin. A square region of interest (ROI) was selected in 10 consecutive slices and the SNR was evaluated as the average gray level over the standard deviation within the same ROI. The measured value was then divided by the SNR computed in the image acquired at the shortest propagation distance (45 mm) and without the application of the phase-retrieval, that resembles a conventional attenuation-based µCT image, hence resulting in the $\mathrm{SNR_{gain}}$. The final $\mathrm{SNR_{gain}}$ values and associated uncertainties were finally computed taking the average and standard error over the 10 measurements.

2.3 Characterization of the system's MTF

Being one input of the previously described model, the pre-sampled imaging system MTF was measured by using the slanted edge method [15, 16] by employing a slightly tilted steel knife-edge target. At every pixel size, N = 100 flat, dark and knife-edge frames were acquired and the MTF was measured on the average flat-fielded image. From the measured MTF, the FWHM of the detector's PSF (parameter d in equation (2.1)) was obtained and used in equations (2.1) and (2.2) to predict theoretical values from the model. Starting from the frequency corresponding to the 10% of the MTF curve ($f_{10\%}$), the spatial resolution was evaluated as the full width at half maximum (FWHM) of the corresponding point-spread function (PSF) [17]:

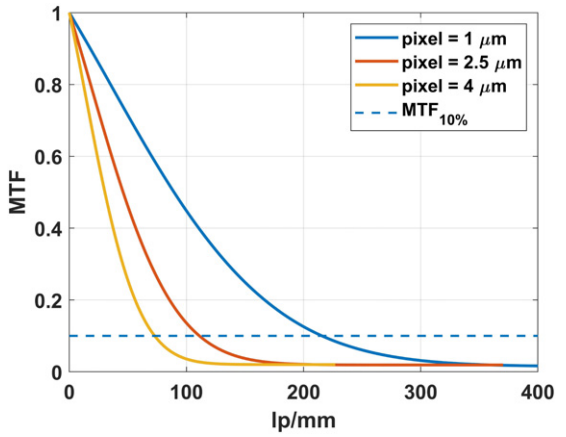

Figure 1. Gaussian fit of detector's MTF and 10% threshold at every pixel size.

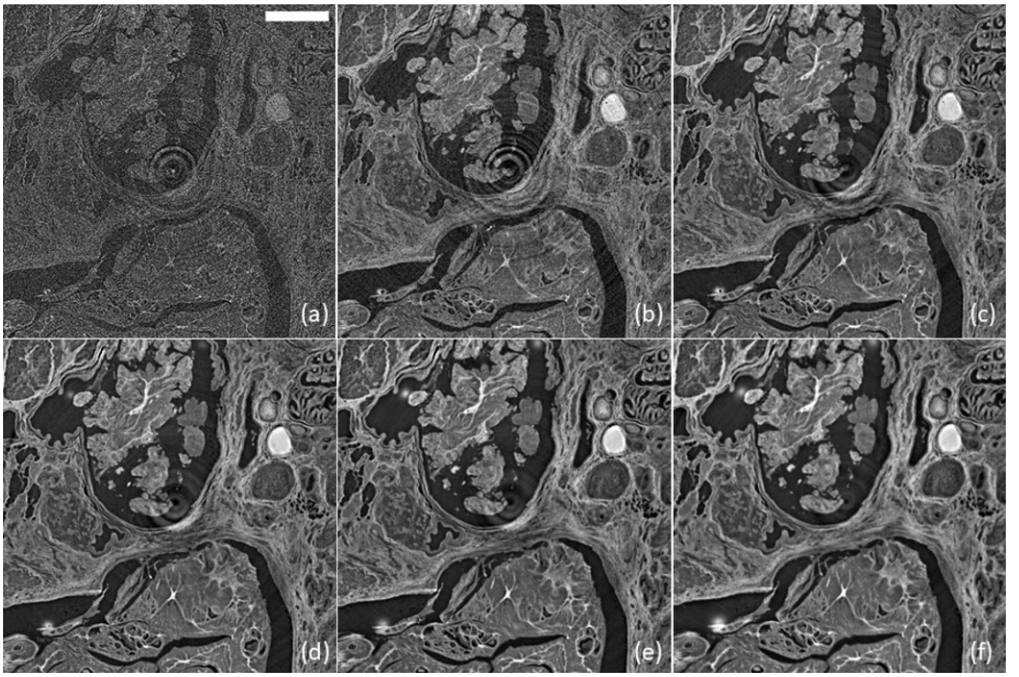

Figure 2. Detail of a slice of the breast specimen acquired with pixel size of 4 µm. Panel (a) shows the detail at 45 mm of propagation distance without the application of phase-retrieval. From (b) to (f) the same detail at propagation distance of 45 mm, 150 mm, 250 mm, 500 mm and 1000 mm, respectively, with the application of PhR. At larger propagation distances, up to 500 mm, a major increase in SNR can be observed. Scalebar in (a) is equal to 1 mm.

$$\text{FWHM (mm)} = \frac{1}{1.24 \times f_{10\%}(lp/\text{mm})} \tag{2.4}$$

where this equation holds in the Gaussian approximation for the PSF (Gaussian fits of the measured MTF curves, at every pixel size, are showed in figure 1). For h = 1.0, 2.5 and 4 µm we obtained d = 3.0, 7.0 and 10.0 µm, respectively.

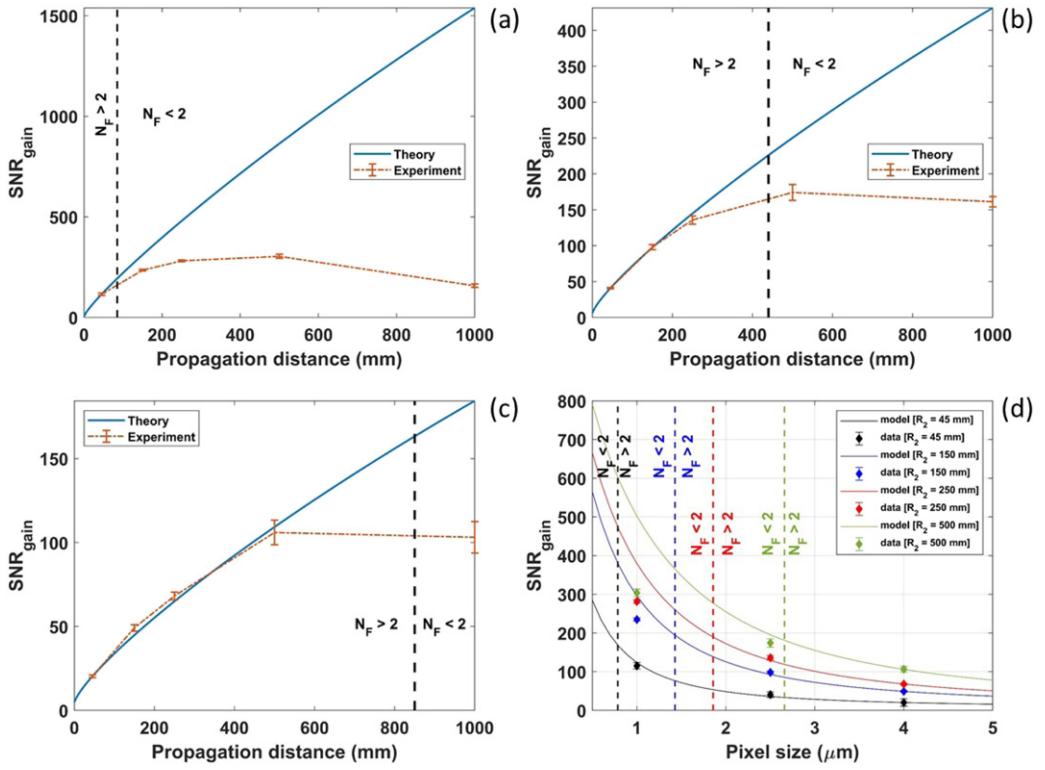

Figure 3. Panels from (a) to (c) show $\mathrm{SNR}_{\mathrm{gain}}$ as a function of the propagation distance for h = 1.0, 2.5 and 4.0 μm, respectively. Blue solid lines are the theoretical predictions while red dot-dashed lines the experimental measurements at propagation distance of 45 mm, 150 mm, 250 mm, 500 mm and 1000 mm. Panel (d) shows the measured $\mathrm{SNR}_{\mathrm{gain}}$ as a function of the pixel size for 45 mm (black), 150 mm (blue), 250 mm (red) and 500 mm (green) propagation distance. A threshold $N_{\mathrm{F}} = 2$ is used for illustration purposes. The departure from the model is observed for $N_{\mathrm{F}} < 2$.

3 Results and discussion

Images obtained at six sample-detector distances using h = 4 μm are shown in figure 2. In figure 2(a) a detail of the image at the shortest propagation distance without the application of PhR is shown, while from (b) to (f) are shown the reconstructions were the PhR is applied. These results indicate that at larger propagation distances, with the application of the PhR algorithm, an increase of the SNR is observed. In fact, for propagation distances up to 500 mm (figure 2(e)), a considerable image quality gain of the detail can be observed.

The plots in figure 3 display, quantitatively, the model results as compared with experimental measurements. Specifically, panels (a)–(c), show the $\mathrm{SNR}_{\mathrm{gain}}$ as a function of the propagation distance at 1.0, 2.5 and 4.0 μm pixel size, respectively. Since the model in equation (2.1) indicates a proportionality between SNR and imaging system related quantities, the theoretical curves have been scaled by a normalization factor such that points at 45 mm of propagation distance match the ones from the experimental measurements. Considering the errors, the experimental results match the $\mathrm{SNR}_{\mathrm{gain}}$ increase predicted by the model when the near field condition is satisfied (a

threshold $N_F = 2$ is used for illustration purposes) as demonstrated by the plots in figures 3(a)–(c). Similar considerations can be drawn in figure 3(d) where the measured SNR_{gain} is plotted against the pixel size for all propagation distances. In all cases deviations between experiment and theory are found when the near-field condition is not fulfilled i.e. ($N_F < 2$). In this framework, while on the one hand the presented analysis allows to validate (in the near-field regine) the theoretical model with polychromatic beam and non-ideal detector, on the other hand allows the optimization of the propagation distance for each pixel size.

At the optimal propagation distance of 500 mm, a morphological comparison between phase-contrast µCT images at 4 µm pixel size and the respective histological image has been performed. The results of the most representative slice is presented in figure 4. The comparison not only reveals a good morphological match between the two techniques, but also an increase in the visibility of the stromal tissue and fibrovascular core (respectively, red curve and green arrows in figure 4(a)) in the µCT acquisition image due to the X-ray phase-contrast imaging modality. Moreover, an intraductal proliferation comprised of arborizing fibrovascular core lined by an outer layer of luminal cells is observed (area enclosed by the orange curve in figure 4(a)). Our images show that high-resolution 3D virtual histology from an unstained soft tissue sample can provide additional information and important feedback to the clinicians in the evaluation of tumour architecture.

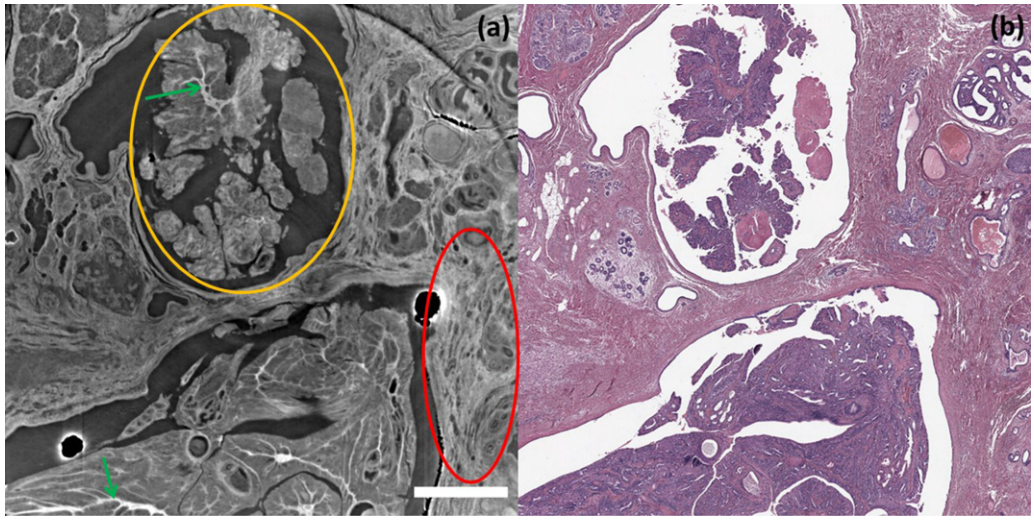

Figure 4. Comparison between X-ray phase-contrast image obtained with 4 µm pixel size (a) and the corresponding histological image obtained with a D-Sight F 2.0 slide scanner (b) of the breast tissue specimen. Red and orange curves enclose, respectively, the stromal tissue and an intraductal proliferation. Green arrows indicate the fibrovascular core. Scalebar in (a) is equal to 1 mm.

4 Conclusions

Experimental results are in good agreement with the theoretical values for the SNR gain associated with the application of the phase retrieval as predicted by the model for Fresnel numbers larger than 2. The model validation has been performed, for the first time, with a synchrotron-generated

polychromatic beam and a commercial imaging system featuring a non-ideal response function. In addition to the model validation, the study performed on the breast sample allowed to find optimal propagation-distance values for each pixel size. This optimization will serve as guideline in the choice of the imaging parameters for a future larger virtual histology study, aiming to assess the invasiveness of malignant diseases in various anatomical districts.

Acknowledgments

This research has been supported by "AIM: Attraction and International Mobility" — PON R & I 2014–2020 Regione Calabria and "Progetto STAR 2" — (PIR01_00008) — Italian Ministry of University and Research.

References

[1] J. Albers, M.A. Markus, F. Alves and C. Dullin, *X-ray based virtual histology allows guided sectioning of heavy ion stained murine lungs for histological analysis, Sci. Rep.* **8** (2018) 1.

[2] J. Albers et al., *X-ray-based 3D virtual histology — adding the next dimension to histological analysis, Mol. Imag. Biol.* **20** (2018) 732.

[3] P. Baran et al., *High-resolution X-ray phase-contrast 3D imaging of breast tissue specimens as a possible adjunct to histopathology, IEEE Trans. Med. Imag.* **37** (2018) 2642.

[4] L. Rigon, *X-ray imaging with coherent sources, Comprehensive Biomed. Phys.* Vol. 2 (2014), pp. 193–220.

[5] L. Brombal, *X-ray Phase-Contrast Tomography: Underlying Physics and Developments for Breast Imaging*, Springer International Publishing (2020).

[6] A. Peterzol, A. Olivo, L. Rigon, S. Pani and D. Dreossi, *The effects of the imaging system on the validity limits of the ray-optical approach to phase contrast imaging, Med. Phys.* **32** (2005) 3617.

[7] T.E. Gureyev, Y.I. Nesterets, A. Kozlov, D.M. Paganin and H.M. Quiney, *On the "unreasonable" effectiveness of transport of intensity imaging and optical deconvolution, J. Opt. Soc. Am. A* **34** (2017) 2251.

[8] D. Paganin, S.C. Mayo, T.E. Gureyev, P.R. Miller and S.W. Wilkins, *Simultaneous phase and amplitude extraction from a single defocused image of a homogeneous object, J. Microsc.* **206** (2002) 33.

[9] L. Brombal et al., *Phase-contrast breast CT: the effect of propagation distance, Phys. Med. Biol.* **63** (2018) 24NT03.

[10] Y.I. Nesterets, T.E. Gureyev and M.R. Dimmock, *Optimisation of a propagation-based X-ray phase-contrast micro-CT system, J. Phys. D* **51** (2018) 115402.

[11] L. Brombal, *Effectiveness of X-ray phase-contrast tomography: effects of pixel size and magnification on image noise,* 2020 *JINST* **15** C01005.

[12] Y.I. Nesterets and T.E. Gureyev, *Noise propagation in X-ray phase-contrast imaging and computed tomography, J. Phys. D* **47** (2014) 105402.

[13] A. Piai et al., *Quantitative characterization of breast tissues with dedicated CT imaging, Phys. Med. Biol.* **64** (2019) 155011.

[14] F. Khan, F. Enzmann and M. Kersten, *Beam-hardening correction by a surface fitting and phase classification by a least square support vector machine approach for tomography images of geological samples,* *Solid Earth Discuss.* **7** (2015) 3383.

[15] H. Fujita et al., *A simple method for determining the modulation transfer function in digital radiography,* *IEEE Trans. Med. Imag.* **11** (1992) 34.

[16] Standard, ISO, *Photography — Electronic Still-Picture Cameras — Resolution Measurements* (2000).

[17] M. Bartels, *Cone-Beam X-ray Phase Contrast Tomography of Biological Samples: Optimization of Contrast, Resolution and Field of View,* Universitätsverlag Göttingen (2013).